A High-Interoperability Optimal Frequency Control Method for the AGV Dynamic Wireless Charging Systems Without Communication

Kaiwen Chen , *Member, IEEE*, Yuzhao Ouyang , Xiaodong Yang ,
Norbert Chow Cheung , *Senior Member, IEEE*, Eric Ka-Wai Cheng , *Fellow, IEEE*,
and Jianfei Pan , *Member, IEEE*

Abstract—In this article, a communication-free optimal frequency control method for the dynamic wireless charging system of automated guided vehicle with high interoperability is proposed. By periodically monitoring the primary winding currents, the position of the receiver (*Rx*) can be located in real-time, and the transmitters which are strongly coupled to the *Rx* will be activated for power transmission. In order to improve the system efficiency, an optimal frequency control scheme for achieving zero-phase-angle is proposed. A proportional-integral loop is employed to achieve quick elimination of the reactive power in primary side. Experimental results show that the positioning and the optimal frequency tuning can be completed within 10 ms. The out-phase can be controlled within 3.57° in the worst case, and the system transfer efficiency is increased up to 11.1%. *Rx*s with different shapes are utilized in experiments as case studies, and the same performance is verified. The results prove the system has high interoperability. Without any bidirectional communication and auxiliary position sensor, the system with the proposed control strategy is proven to be reliable and eco-friendly.

Index Terms—Automated guided vehicle (AGV), dynamic wireless power transfer, optimal frequency control (OFC).

I. INTRODUCTION

AUTOMATED guided vehicles (AGVs) have been widely utilized for freight transport, with the aim of labor reduction, through transportation electrification [1], [2], [3]. The charging methods for these AGVs can be basically classified into cabled charging and wireless charging. Although the traditional cabled AGV charging has high efficiency, there are several drawbacks, which are as follows.

1) Frequent plugging and unplugging of the connectors increases the chance of electrical hazards.
2) At least one backup group of AGV is needed, which increases system cost.
3) The stop-to-charge operation limits the working hours of the AGVs.

Wireless charging, which contributes to a better electric-isolated energy transmission, is becoming an ideal alternative than cabled charging [4], [5], [6], [7], [8]. In terms of the receiver (*Rx*) motion, the wireless charging method can be divided into static wireless charging and dynamic wireless charging (DWC). In order to solve the above mentioned problem, the DWC system, which allows the *Rx*s to be charged when they are moving, is proved to be a more feasible solution, because the battery packs can be reduced and the working time of the AGVs will be extended [9], [10], [11].

However, there are several issues that limit the implementation of DWC system for AGVs which are as follows.

1) The variations of coupling condition brought by misalignment between grid-side transmitters (*Tx*s) and AGV-side *Rx*s cause a large amount of reactive power, which decreases the power factor and system efficiency.
2) The considerable monitoring time of the control loop does not match the fast movement of AGVs.
3) The utilization of different kinds of AGVs challenges the interoperability of DWC system.

In order to optimize the efficiency in DWC systems, several control methods have been introduced. These methods could be classified into three categories, namely coupler optimization (CO) [12], [13], [14], [15], [16], phase-shift control (PSC) [17], [18], [19], and optimal frequency control (OFC) [20], [21], [22], [23], [24], [25]. The CO schemes, includes coil optimization [12], [13] and compensation network optimization [14], [15], [16], are passive in implementation, and the CO schemes are commonly operational in limited operation condition. Although the variation of the coupling coefficient could be damped, there are still reactive power generated when the *Rx* moves out of the valid range.
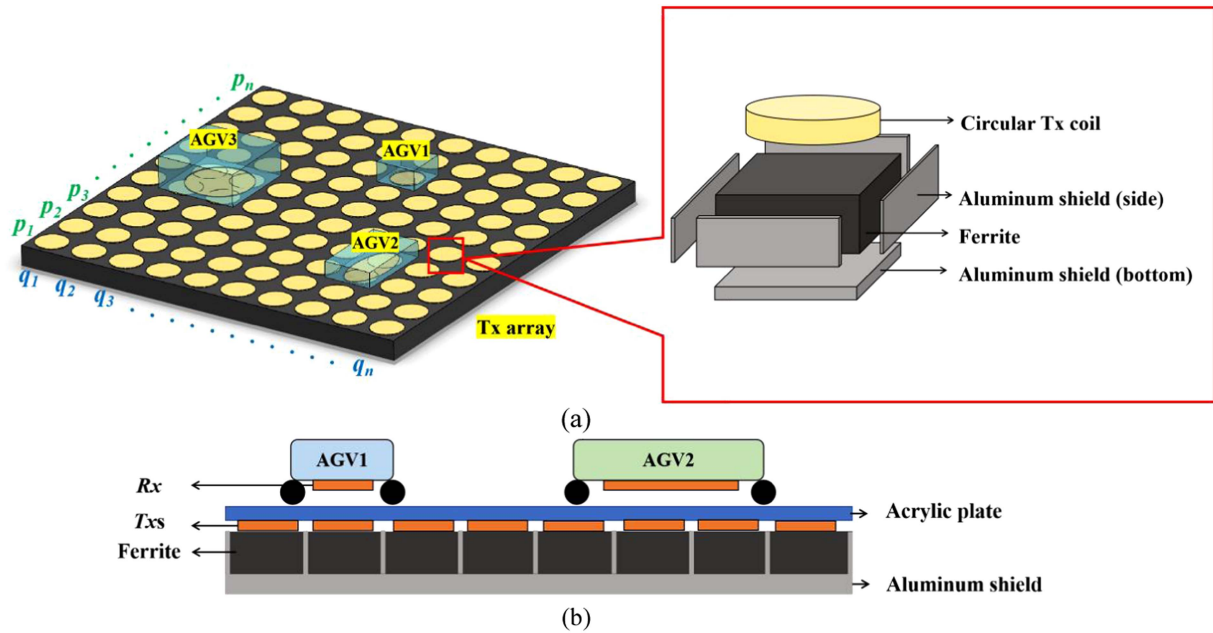
Fig. 1.   (a) Configuration of the proposed DWC system for AGVs and explosive view of the *Tx* module. (b) Side view of the DWC platform.

The PSC scheme indicates that the primary winding voltage is adjusted based on the estimated coupling coefficient. A DWC system with optimized efficiency control is proposed in [17]. By adopting a bidirectional communication module for real-time delivering load condition, the optimized impedance in each primary winding is estimated, and the winding voltage is determined accordingly. However, the communication module enlarges the monitoring time in control cycle, and the handshake process could decrease the reliability of the system. To solve this problem, a perturb and observe (P&O) scheme for optimized efficiency and output voltage regulation is proposed in [18]. Although the communication and position sensor is excluded, it still needs a large amount of calculation effort which leads to long sweeping delay and dynamic response. Through the adoption of switching frequency tuning, the OFC scheme could realize high efficiency operation with the regulation of the power factor. In [20], the optimal frequency is proved to exist in a wide frequency band and different coupling conditions. By tracking the optimal frequency, the reactive power could be reduced. A frequency tuning method is proposed in [19] and [21], but an extra communication unit between the *Tx*-side and the *Rx*-side is required. The P&O scheme is employed for optimal frequency tracking in [22]. This system has the advantage of communication-free. However, the proposed method requires heavy calculation. An OFC method for achieving maximum power output in 1-to-1 WPT system is proposed in [23]. Although no additional communication unit is introduced, the method is feasible with constant coupling condition in charging mode. In [24], the optimal frequency is estimated by calculating the apparent power and the active power. However, a complex circuit is needed and the calculation effort is significantly large. A digital circuit for directly detection of the out-phase for the optimal frequency is proposed in [25]. Nevertheless, the frequency-sweeping method increases the detecting time. Based on the general review of the above literature, it can be

concluded that both the OFC scheme could achieve optimized efficiency operation by satisfying zero phase angle (ZPA) in primary side [26], and the PSC can even achieve maximum efficiency tracking. However, the traditional control methods require either extra bidirectional communication hardware or complicated parameter estimation computation load, which limits the dynamic performance of the DWC system. Besides, the conventional OFC based on P&O only allows one frequency sweeping direction, which may lead to failure in finding the optimal frequency because the multi-*Tx*s DWC system has either inductive or capacitive resonance condition. Hence, for AGV DWC systems, not only the dynamic performance needs to be considered for matching the AGV velocity, but also the control method should be simple and reliable.

In this article, a communication-free positioning and OFC method for AGV DWC systems is proposed. Based on a typical DWC system configuration with multiple *Tx*s (multi-*Tx*s) in [27], a matrix configuration of *Tx*s is introduced in this article for generating enough electromagnetic field for randomly moving AGVs. The position of the *Rx* is real-time located by detecting the primary current, and *Tx*s which are strongly coupled with the *Rx* will be activated in power transmission. A simple digital circuit is introduced to recognize the resonance condition of the primary side, and the frequency sweeping direction can be determined. An OFC scheme is proposed for achieving ZPA, and the proportional-integral (PI) loop is integrated for improving the dynamic performance. The main contributions of this article can be summarized as follows.

1) *Recognizable resonance conditions*: The inductive and capacitive resonance conditions can be recognized by a simple digital circuit, and thus the frequency sweeping direction can be determined without complicated parameter estimation.

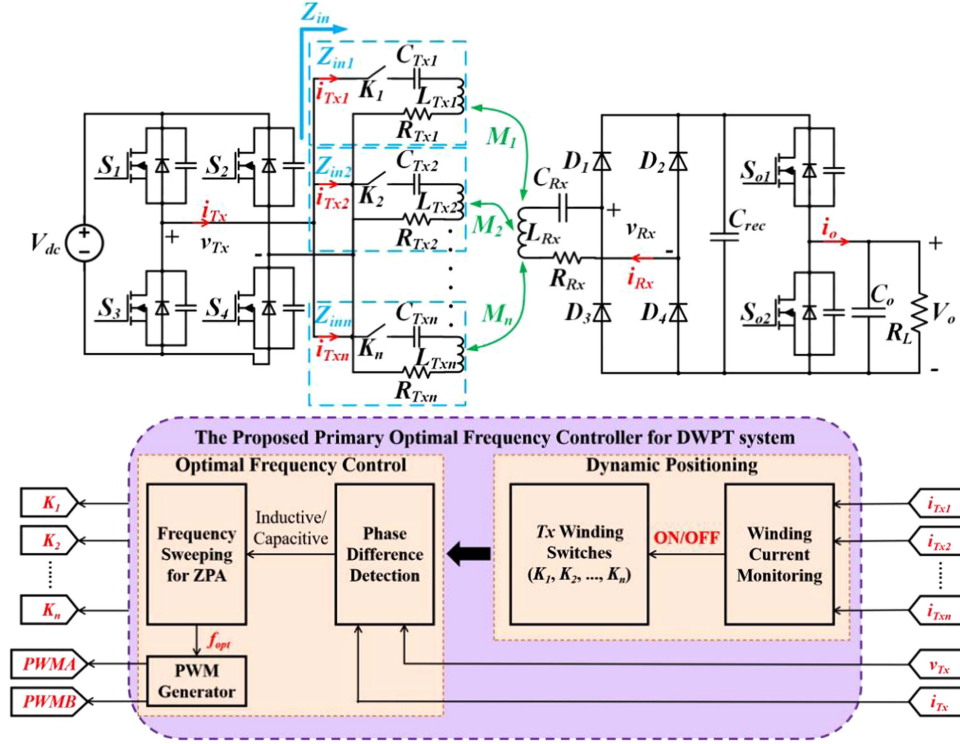2) *Fast dynamic performance*: No communication and auxiliary position sensor is required in the positioning

Fig. 2. Circuit topology of multi-*Txs* SS compensated WPT system.

process, and a PI loop is introduced to improve the dynamic response. The proposed positioning and OFC can be completed in several milliseconds.

3) *High interoperability*: The proposed system is able to charge AGVs with different *Rx*s in movement. The moving directions of the AGVs can also be random.

II. SYSTEM MODELING AND IMPLEMENTATION OF THE POSITIONING SCHEME

A. System Modeling and Principles of the Positioning Scheme

A multi-*Txs* series-series compensated (SS-compensated) DWC system for AGVs is constructed. Fig. 1(a) shows the configuration of the proposed system and the explosive view of each *Tx* module, and its side view is depicted in Fig. 1(b). The aluminum shield on the bottom is utilized to avoid electromagnetic interference to the surroundings, and that on the side surface is to minimize the cross coupling between *Tx*s. The system is covered with ferrite to enhance the coupling performance. Multiple circular *Tx* coils with the same spacing and size are constructed for energizing the electromagnetic field for power transmission. Each *Tx* coil is labeled with row (i.e., q) and column (i.e., p). AGVs with different sizes of *Rx*s is to be charged while moving on the work platform.

The equivalent circuit of the system is presented in Fig. 2. The *Tx*s (i.e., L_{Tx1}–L_{Txn}), are driven by a full-bridge inverter (i.e., S_1–S_4) where V_{dc} is the input direct current (dc) voltage. C_{Tx1}–C_{Txn} are the compensated capacitors for the *Tx*s. Z_{in} represents the input impedance, which is calculated by the input alternating current (ac) voltage and current (i.e., v_{Tx} and i_{Tx}).

The equivalent series resistance (ESR) of L_{Txj} and C_{Txj} is represented by R_{Txj}. The selected *Txs* are activated by turning ON their winding selective switches (i.e., K_1–K_n), which are controlled by a digital signal processor (DSP). At the same time, S_1–S_4 are also controlled by the same DSP (S_1, S_4 by PWMA and S_2, S_3 by PWMB), and a high-frequency EMF is thus generated. The *Rx* resonator consists of an inductive coil L_{Rx} and its compensated capacitor C_{Rx}. M_1–M_n are the mutual inductance between L_{Tx1}–L_{Txn} and L_{Rx}, respectively. There is also mutual inductances between the *Tx*s, and they are measured on the experimental platform. The mutual inductance between two adjacent transmitters only accounts for no more than 2% of their self-inductance. In order to simplify the model, those mutual inductances have been neglected. The ESR in the *Rx* resonator is expressed as R_{Rx}. v_{Rx} and i_{Rx} is the resonator voltage and current of the *Rx*, respectively. The diode rectifier (i.e., D_1–D_4) feeds the AGV loads (i.e., R_L) with dc output voltage, V_o. A regulator C_o is employed to filter the ac components.

The primary winding voltage can be expressed as follows:

$$v_{Tx} = Z_{Txj}\, i_{Txj} - i\omega M_j i_{Rx} \tag{1}$$

where i_{Txj} is the winding current in coil j, M_j is the mutual inductance between the L_{Txj} and L_{Rx}. $\omega = 2\pi f$ is the angular frequency, and f is the switching frequency of the inverter. Z_{Txj} is the impedance of resonator j, which can be expressed as follows:

$$Z_{Txj} = R_{Txj} + i\left(\omega L_{Txj} - \frac{1}{\omega C_{Txj}}\right). \tag{2}$$

On the *Rx*-side

$$Z_{Rx}i_{Rx} - i\omega M_j\, i_{Txj} = 0 \tag{3}$$

where Z_{Rx} is the impedance of the *Rx*, and it can be calculated as follows:

$$Z_{Rx} = R_{\text{eq}} + i\left(\omega L_{Rx} - \frac{1}{\omega C_{Rx}}\right). \tag{4}$$

By combining the (1)–(4), the input impedance of one primary winding could be expressed as follows:

$$\frac{v_{Tx}}{i_{Txj}} = R_{Txj} + i\left(\omega L_{Txj} - \frac{1}{\omega C_{Txj}}\right) + \frac{\omega^2 M_j^2}{Z_{Rx}}. \tag{5}$$

The self-inductance of the *Tx* coil increases with the alignment of the *Rx* due to lower magnetic resistance [29]. At the same time, the mutual inductance between L_{Txj} and L_{Rx} rises due to stronger coupling. An increment of L_{Txj} and M_j causes a reduction of i_{TXj}

$$\frac{v_{Tx}}{i_{Txj} - \Delta i_j} = R_{Txj} + \left|\omega\left(L_{Txj} + \Delta L_j\right) - \frac{1}{\omega C_{Txj}}\right|$$
$$+ \frac{\omega^2(M_j + \Delta M_j)^2}{Z_{Rx}} \tag{6}$$

where ΔL_j, ΔM_j, and Δi_j are the variation of L_{Txj}, M_j, and i_{TXj}, respectively. Thus, Δi_j can be expressed as follows:

$$\Delta i_j = \left|\frac{i_{TXj}Z_{Rx}\omega\Delta L_j + \omega^2(2M_j\Delta M_j + \Delta M_j)^2}{Z_{Txj}Z_{Rx} + \omega\Delta L_j Z_{Rx} + \omega^2(M_j + \Delta M_j)^2}\right|. \tag{7}$$

Hence, it is possible to determine the location of the *Rx* only by detecting the variation of the *Tx* winding currents. There is no need for any communication between the *Tx*-side and the *Rx*-side. The mutual inductance between a *Tx* and the *Rx* increases with the decrease in the distance, and the winding current decreases in this process. Therefore, the *Tx*-side can locate the receiver regardless of its shape, and a high interoperability is thus ensured. Besides, the transmitters are in circular shape, they generate uniform distribution of EMF and are arranged in matrix form. Therefore, the moving directions of AGVs are not limited.

B. Implementation of Dynamic Positioning

In the charging process, if all the *Txs* are activated for transferring power, there will be a considerable power loss in the winding impedance of the weakly coupled *Txs*. Activating strongly coupled *Txs* for transferring power can significantly improve the total system efficiency. Therefore, it is necessary to detect the current in each *Tx* to determine the position of the *Rxs*. The schematic waveform of the active-positioning process is shown in Fig. 3(a). $\hat{i}_{Tx}$ represents the peak value of i_{Tx}. For determining the coupling condition of the *Txs* and *Rx*, the *Txs* will be energized in sequence. The $\hat{i}_{Tx}$ of each energized *Tx* coil is monitored and compared with the threshold value φ. The $\hat{i}_{Txj}$ indicates the *Rx* covered area, and the coupling coefficient between the *Tx* and *Rx* is also proportional to the coverage ratio. This relationship has been verified by experiment, and the *Rx* is placed to cover one of the *Txs* in different coverage with an
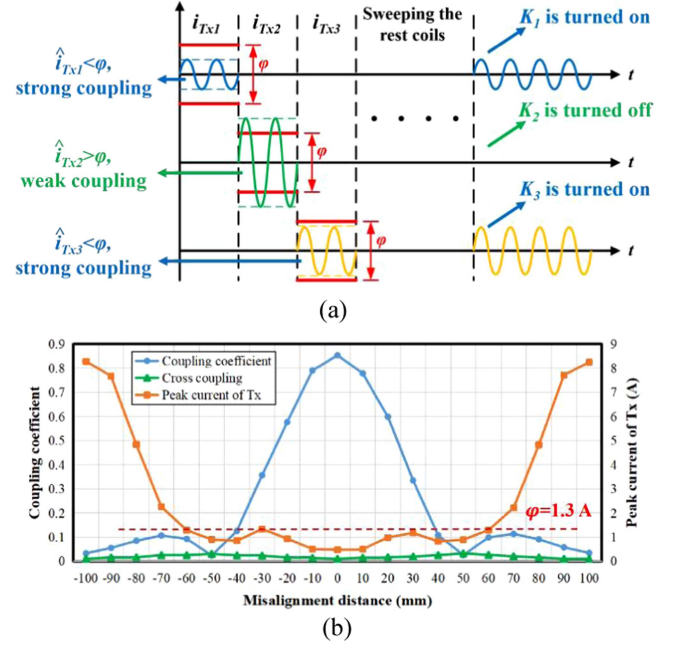

Fig. 3. (a) Schematic timing diagram of the winding current in the active-positioning process. (b) Relationship between the peak current of the *Tx* winding and coupling coefficient.

air gap of 7 mm. The results are demonstrated in Fig. 3(b). It can be observed that here is a undesired coupling impulse when the misalignment is larger than 60 mm. In order to avoid the influence brought by the impulse of coupling coefficient, the threshold value is determined to be 1.3 A. The *Txs* with $\hat{i}_{Txj}$ lower than φ will be selected in the charging period, which indicates that the *Txs* with higher than 0.15 coupling coefficient will be activated in the charging stage. The coupling between the inactive *Txs* and *Rx* will not be involved in the optimal frequency control and the normal charging progress. For instance, in Fig. 3(a), the $\hat{i}_{Tx1}$ and $\hat{i}_{Tx3}$ are lower than φ, which indicates a strong coupling with the *Rx* coil. Meanwhile, L_{Tx2} is detected to be weak-coupled with the *Rx* coil. Hence, K_1 and K_3, which are the active switches for *Tx1* and *Tx2*, are turned ON in the charging period. The cross coupling between *Txs* is minimized by the aluminum shields in the side surface of the *Tx* modules. As can be observed from Fig. 3(b), the maximum cross coupling is lower than 0.03, which is much smaller than the coupling coefficient between *Tx* and *Rx*. Hence, it does not influence the control process in this study.

In the initial sweeping period, all *Txs* will be energized in sequence, and the *Txs* with $\hat{i}_{Tx}$ lower than φ will be marked. When the sweeping process is finished, the selected switches will be turned on and their corresponding *Tx* coil will be activated. After the initial sweeping period, the locations of the *Rxs* will be recorded.

In order to reduce power loss and shorten the control period, a sweeping strategy is utilized. Instead of sweeping all *Txs* on the platform, only the *Txs* adjacent to the coils selected in the last period will be swept in the subsequent period, as shown in Fig. 4(a). For example, if the *Rx* coil has the same size with the
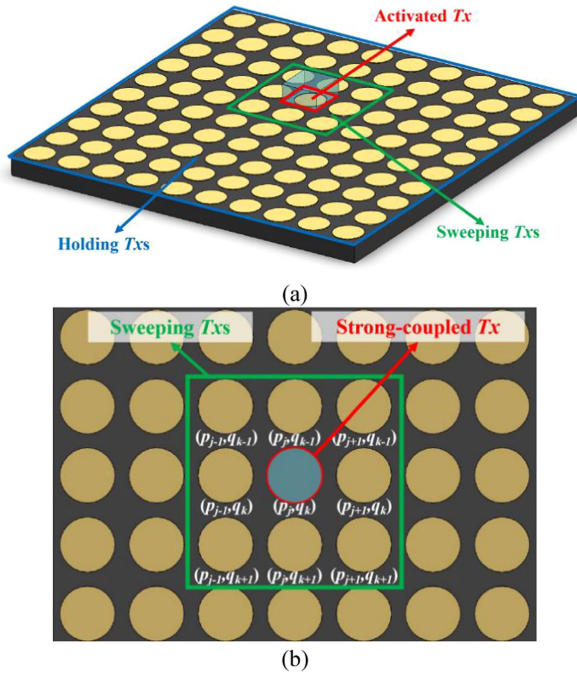
Fig. 4. (a) *Txs* status in the proposed positioning strategy. (b) Sweeping *Txs* for coupling condition monitoring.

Fig. 5. Flowchart of the positioning scheme.

Txs, and it is aligned with a *Tx* coil marked (p_j, q_k), only the (p_j, q_k) will be energized after the last sweeping period. Then in the next period, only coils (p_a, q_b) $(0 \leq j{-}1 \leq a \leq j{+}1 \leq m, 0 \leq k{-}1 \leq b \leq k{+}1 \leq n)$ will be swept, as depicted in Fig. 4(b). This strategy avoids redundant power loss as well as shorten the period of the detecting process. Fig. 5 demonstrates the flowchart of the practical active positioning implementation.

III. PROPOSED OFC METHOD FOR EFFICIENCY OPTIMIZATION

A. Feasibility Analysis of the OFC Scheme

With the AGV moves, the self-inductance of the *Txs* are influenced, and the resonant frequencies are changed. The reactive power generated in the system reduces the transfer efficiency, and it is impossible to guarantee a high efficiency only by the active-positioning. In [24] and [30], by realizing ZPA, the active power in windings can be maximized, and the system efficiency is thus increased. In order to maximize the active power and to improve the power factor, a frequency control scheme is utilized after the active-positioning process in a controlling period. For a certain coil *j*, the input equivalent impedance is as follows:

$$Z_{\text{inj}} = \frac{v_{Tx}}{i_{Txj}} = R_{Txj} + jX_{\text{inj}}. \tag{8}$$

According to the research in [26] and [32], the reactance of Z_{inj} can be expressed as follows:

$$X_{\text{inj}} = \omega L_{Txj} \left[1 - \frac{\omega_{Txj}^2}{\omega^2} - \frac{k_j^2}{1 - \frac{\omega_{Rx}^2}{\omega^2}} \right] = |Z_{\text{inj}}| \sin\theta_j \tag{9}$$

where ω_{Txj} and ω_{Rx} are the resonant angular frequencies of the *Tx* coil *j* and the *Rx* coil, respectively. θ_j is the phase difference
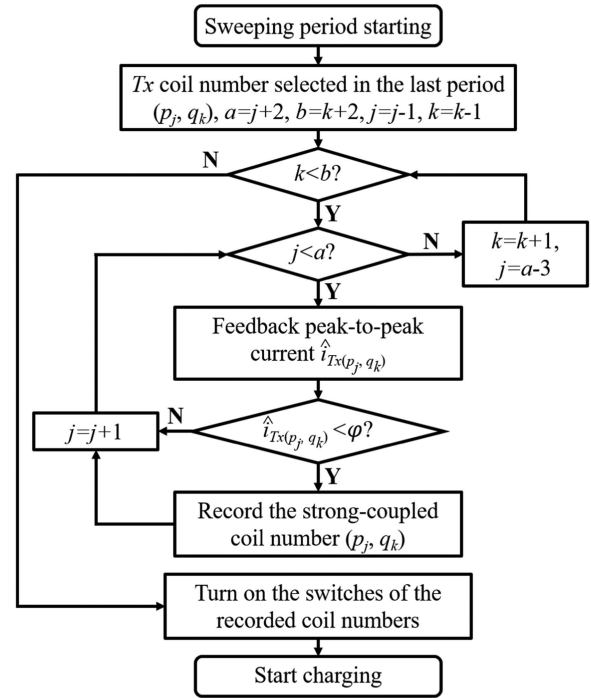
between v_{Tx} and i_{Txj}, and k_j is the coupling coefficient of L_{Txj} and L_{Rx}

$$k_j = \frac{M_j}{\sqrt{L_{Txj} L_{Rx}}}. \tag{10}$$

To eliminate the phase difference θ_j, it can be deduced that

$$\left(1 - k_j^2\right) \omega^4 - \left(\omega_{Txj}^2 + \omega_{Rx}^2\right) \omega^2 + \omega_{Txj}^2 \omega_{Rx}^2 = 0. \tag{11}$$

There are two zeros of (11), including ω_{cj} in the capacitive zone and ω_{lj} in the inductive zone, respectively

$$\omega_{cj} = \sqrt{\frac{\omega_{Txj}^2 + \omega_{Rx}^2 - \sqrt{\left(\omega_{Txj}^2 - \omega_{Rx}^2\right)^2 + 4k_j^2\omega_{Txj}^2\omega_{Rx}^2}}{2\left(1 - k_j^2\right)}} \tag{12}$$

$$\omega_{lj} = \sqrt{\frac{\omega_{Txj}^2 + \omega_{Rx}^2 + \sqrt{\left(\omega_{Txj}^2 - \omega_{Rx}^2\right)^2 + 4k_j^2\omega_{Txj}^2\omega_{Rx}^2}}{2\left(1 - k_j^2\right)}}. \tag{13}$$

Due to the random movement of the AGV, there is always a misalignment between the *Tx* and the *Rx* coil. According to the analysis in [24], the capacitive reactance increases with the misalignment, while the inductance reactance reaches the maximum when the coils are in alignment. To reduce the impedance in the case of *Rx* misaligning, the system should be tuned to the optimal frequency ω_{lj}, in order to ensure the *Tx*-side works in the inductive zone. When the operating frequency ω_o is equal to ω_l, the phase difference φ_j will be eliminated, and a high efficiency can be achieved. The self-inductance of the *Txs* will
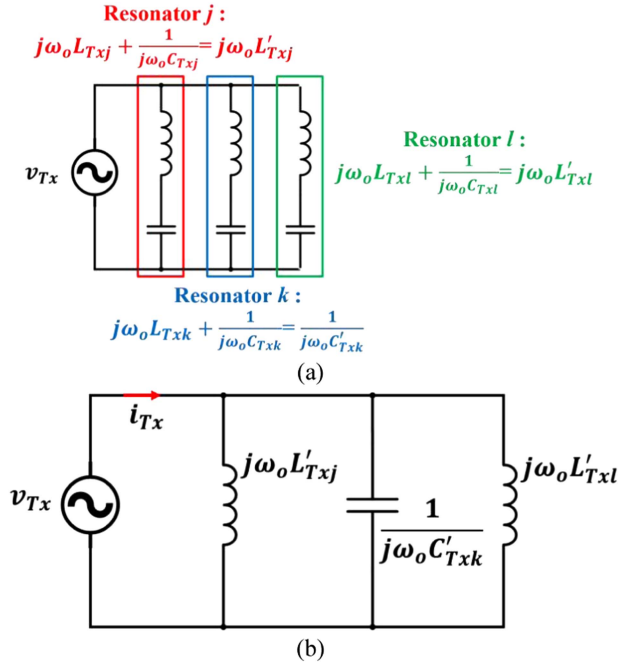
Fig. 6. (a) Status of each resonator under a certain operating frequency. (b) Equivalent circuit of the *Tx*-side.
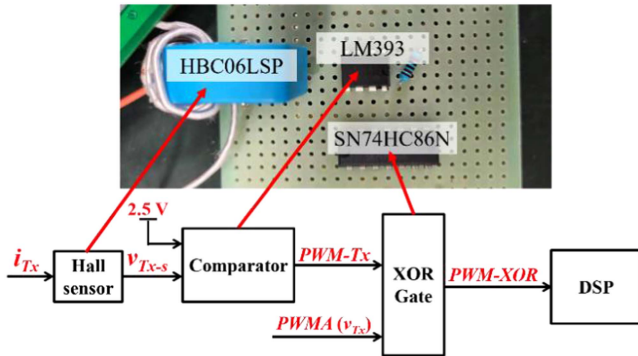

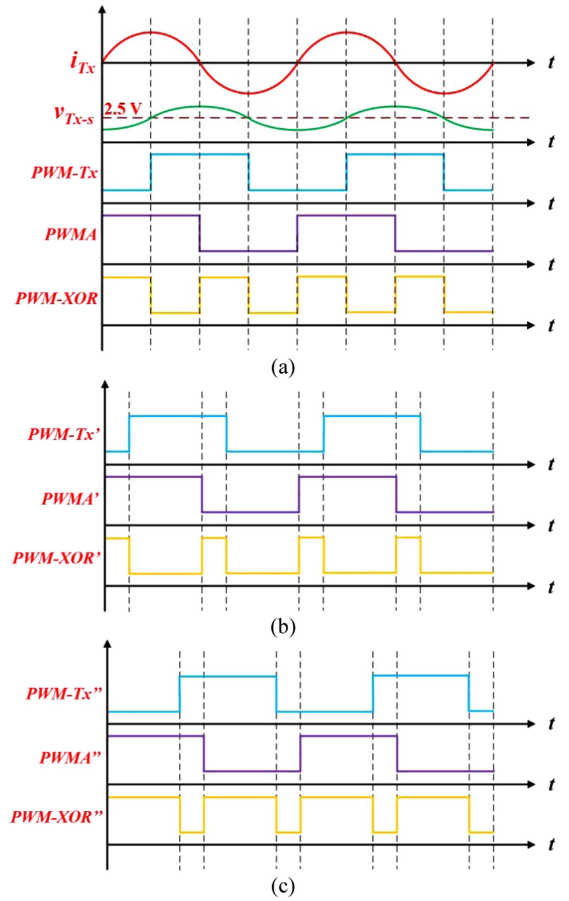Fig. 7. Digital circuit for phase difference monitoring.

Fig. 8. Diagram of the out-phase monitoring. (a) i_{Tx} is in-phase with v_{Tx}. (b) i_{Tx} is ahead of v_{Tx}. (c) i_{Tx} is lagging behind v_{Tx}.

By tuning the operating frequency to ω_{opt}, the phase difference between v_{Tx} and i_{Tx} will be eliminated, the optimized efficiency can be achieved.

B. Implementation of Efficiency Optimized Control

The tuning of switching frequency can be conventionally achieved by the P&O scheme [22] and the parameter estimation [25]. However, the tuning period is usually considerable due to either sweeping time or complicated calculation, which does not match the fast movement of AGVs. In order to improve the dynamic response of the control loop, a PI controller is proposed based on the traditional P&O scheme for achieving ZPA.

For detecting the phase difference in a reliable and cost-effective way, a low-cost digital circuit is utilized, and the detailed structure of this digital circuit is depicted in Fig. 7. The Hall current sensor (HBC06LSP) is employed to detect the ac primary current i_{Tx}, and it outputs a sinusoidal dc signal voltage v_{Tx-s}. v_{Tx-s} has the same frequency as i_{Tx}, but its phase lags by 90°. The amplitude of v_{Tx-s} is 0–5 V, by comparing with a dc voltage of 2.5 V in a comparator (LM393), a PWM signal (PWM-*Tx*) will be created. PWMA of the inverter is in-phase with the input voltage v_{Tx}, but it has a standard voltage of 0–3.3 V and is stabler. Therefore, PWMA is utilized

be influenced when the receiver moves. Due to the constant compensation capacitors, the resonant frequency of each resonator would be changed dynamically. Some of them will be inductive and others will be capacitive. Therefore, there is a frequency that can realize ZPA for the whole paralleled transmitter resonators. In the proposed system, several windings will be energized after the active-positioning sweeping. For a proper ω_o, resonators with a resonant frequency higher than ω_o work in the capacitive zone, while the others work in the inductive zone. As presented in Fig. 6(a), the resonator *j* and *l* are inductive and *k* is capacitive, if they share the same operating frequency ω_o. The equivalent circuit topology of this condition is shown in Fig. 6(b).

Because the resonators are parallel-connected to the inverter, an optimal frequency ω_{opt} is used to realize the equation:

$$j\omega_{\text{opt}}L'_{Txj} + \frac{1}{j\omega_{\text{opt}}C'_{Txk}} + j\omega_{\text{opt}}L'_{Txl} = 0. \tag{14}$$

(a)

(b)

Fig. 9. Implementation of the proposed OFC scheme. (a) Closed-loop diagram. (b) Flowchart of the OFC scheme.

(a)

(b)   (c)

Fig. 10. (a) Experimental platform of the proposed system. (b) Rx-I (circular). (c) Rx-II (oval).

to represent v_{Tx} in the phase detecting for more accuracy. PWM-*Tx* and PWMA will be fed to an Exclusive-OR (XOR) gate (SN74HC86N) together, and the feedback signal PWM-XOR will be generated and sent to the DSP.

Fig. 8(a) shows the timing diagram of the aforementioned signals (i.e., i_{Tx}, v_{Tx-s}, PWM-*Tx*, PWMA, and PWM-XOR) when i_{Tx} is in-phase with v_{Tx} (represented by PWMA). The duty-cycle of PWM-XOR (Dp) is 50% in this case. It decreases when i_{Tx} is ahead of v_{Tx}, and increases when i_{Tx} legs behind, as presented in Fig. 8(b) and (c). Therefore, the phase difference between i_{Tx} and v_{Tx} can be reflected by the output of this simple digital circuit, and the leading and delaying of i_{Tx} can also be distinguished. As long as the duty cycle Dp is controlled at 50%, the phase difference between v_{Tx} and i_{Txj} can be eliminated.

After the PWM-XOR is sent to the DSP, since the PWM-XOR is a 1/0 signal, the rising edge and falling edge triggered interrupt system of DSP is utilized to recorded pulsewidth time of Dp, and it is divided by the cycle time to get the duty cycle of Dp. By subtracting Dp from the target value of 50%, the error is obtained and fed to a PI controller. The switching frequency can be thus calculated and sent to the full-bridge inverter. By adjusting the switching frequency, Dp can be controlled to maintain 50% duty cycle, which indicates that the ZPA is achieved between i_{Tx} and v_{Tx}. The control flowchart is demonstrated in Fig. 9(a), and the detail implementation of the OFC scheme is drawn in Fig. 9(b).

IV. EXPERIMENTAL VERIFICATION

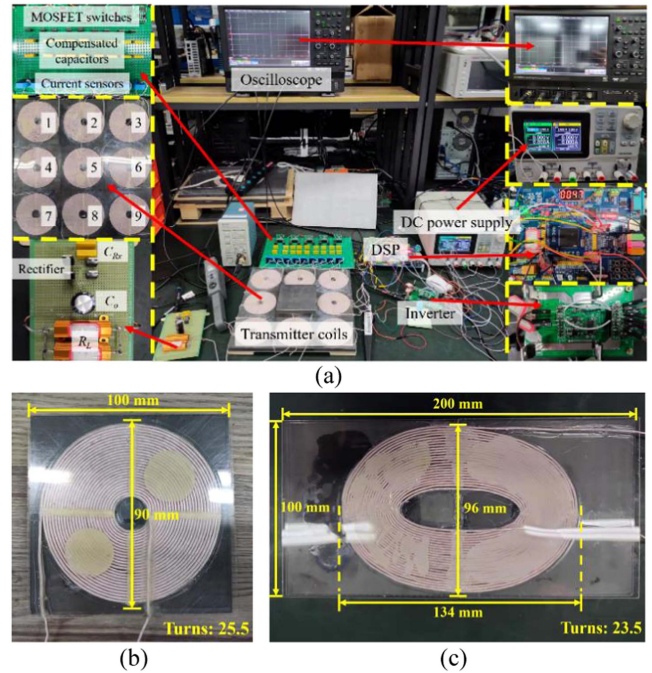The experimental platform of this article is depicted in Fig. 10(a). The system is powered by SIGLENT SPD3303X programmable dc power supply. The *Tx* array contains nine circular coils with 25.5 turns and radius of 45 mm, and these coils are marked from 1–9, respectively. The size of ferrite in the *Tx*-side is 300 mm × 300 mm × 10 mm, and the aluminum shield is 300 mm × 300 mm × 2 mm. The winding currents of the *Tx* coils are monitored by HBC06LSP hall sensors and fed to the DSP. The DSP for the *Tx*-side control is TMS320F28335. The MOSFETs of the inverter and the gate switches are IRF740. The waveforms are captured by an oscilloscope. The parameters of the components, such as L_{Tx}, C_{Tx}, and R_{Tx} are measured by LCR Meter under the operating frequency of 100 kHz, and are listed in Table I. To verify the interoperability of the proposed system, two shapes of *Rx* coils (namely *Rx-I* and *Rx-II*) are employed, as shown in Fig. 10(b) and (c). *Rx-I* has the same size with the *Tx* coils, it carries a ferrite block of 100 mm × 100 mm × 10 mm and an aluminum shield of 100 mm × 100 mm × 1 mm. *Rx-II* has an oval coil with 23.5 turns, and the size of its ferrite block and aluminum shield are 200 mm × 100 mm × 10 mm and 200 mm × 100 mm × 1 mm, respectively.

A. Verification of the Positioning Scheme

For the positioning process, the system input dc voltage V_{dc} is set at 24 V and its resonant frequency is 100 kHz. As shown in Fig. 11(a)–(c), the *Rx-I* is put in three different initial positions in the *Tx* array: at the corner (i.e., zone 9), along the sideline (i.e., zone 8) and in the center (i.e., zone 5). In order to verify the dynamic active-positioning scheme, the *Rx-I* is moved in two different directions, which are straight and diagonal directions. When an active-positioning period starts, *Txs* in the determined sweeping zone will be energized in sequence, and the coils have a strong coupling with the *Rx* will be activated for power
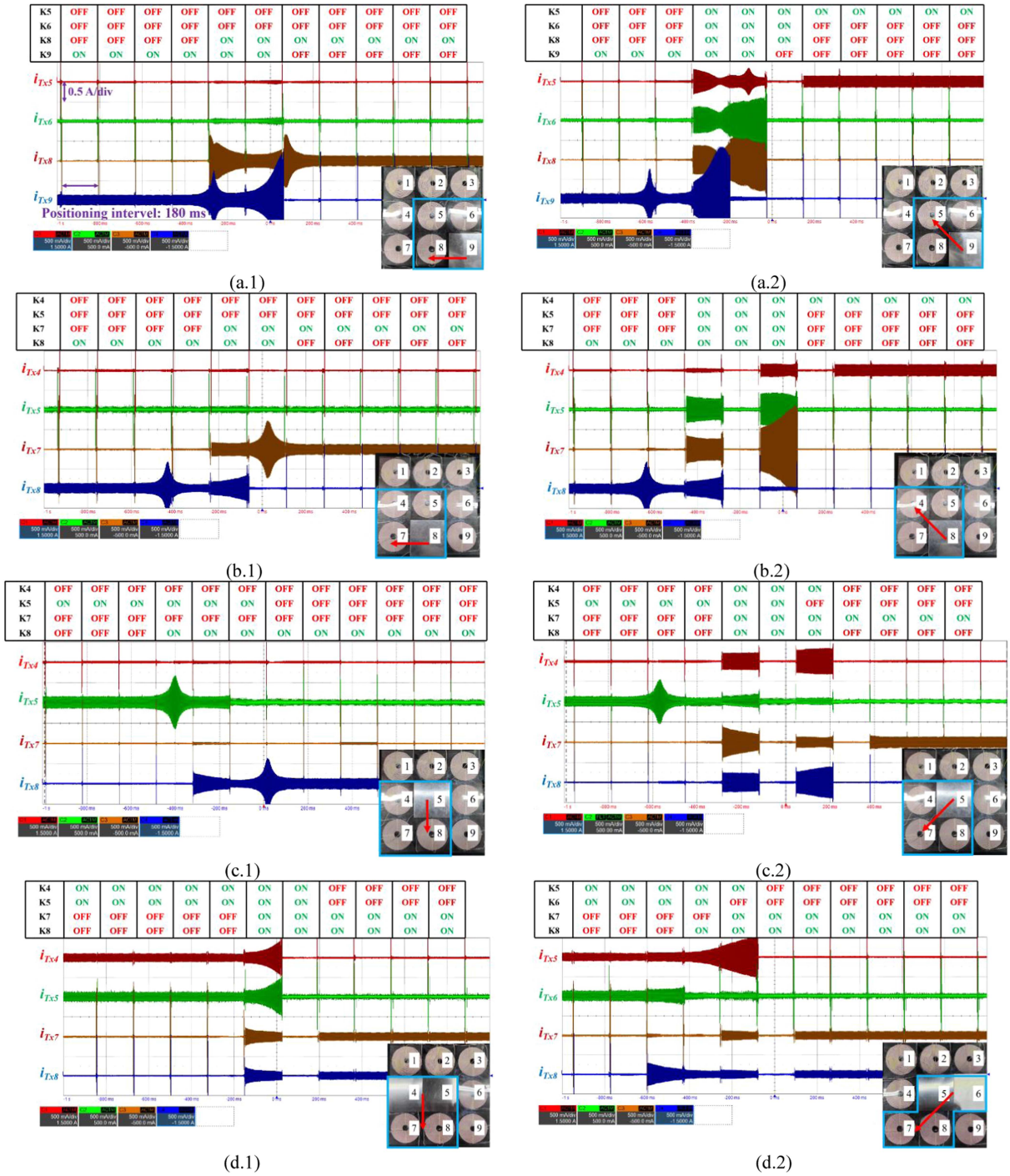
Fig. 11. Experimental waveforms of the active-positioning control with different movement and placement of *Rxs*. (a) *Rx-I* moves from the corner. (b) *Rx-I* moves from the sideline. (c) *Rx-I* moves from the center. (d) *Rx-II* moves from the sideline; (x.1) straightly, (x.2) diagonally.

transmission. The detection of each coil takes merely 0.4 ms, as demonstrated in Fig. 12. The scale of the oscilloscope is 1 ms/div in time and 0.5 A/div in current. The winding current results in the active-positioning process are depicted in Fig. 11(a) to (c). The scale of the oscilloscope is 200 ms/div in time and 0.5 A/div in current, and the positioning interval is 180 ms.

As presented in Fig. 11(a.1), the *Rx-I* moved from zone 9 to zone 8 straightly, the red array represents the moving direction. Coil 9 is energized and coil 8 is cut off in the beginning. While

the *Rx-I* is moving, $\hat{i}_{Tx5}$, $\hat{i}_{Tx6}$, $\hat{i}_{Tx8}$, and $\hat{i}_{Tx9}$ are monitored and compared to φ. In this process, when $\hat{i}_{Tx8}$ is lower than φ, coil 8 will be activated and K_9 will be turned OFF when $\hat{i}_{Tx9}$ is higher than φ. As shown in Fig. 11(a.2), when the *Rx-I* moves from zone 9 to zone 5 diagonally, $K9$ will be turned OFF from ON, and coil 5 will be activated when $\hat{i}_{Tx5}$ is lower than φ. In this process, coil 6 and coil 8 will be energized for a short time when the *Rx-I* is moving close to them. Similar results of the other two placements are drawn in Fig. 11(b) and (c).

TABLE I
KEY PARAMETERS (MEASUREMENT CONDITION: 100 KHZ, 25 °C)

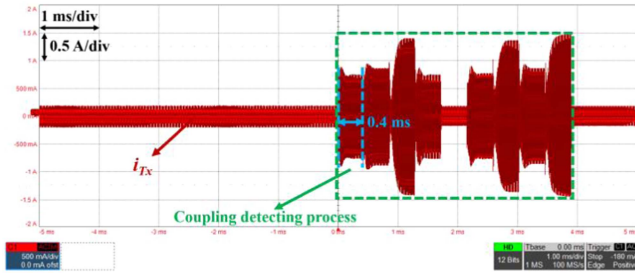|	Symbol	Value	Symbol	Value	Symbol	Value
	L_{Tx1}	52.17 μH	C_{Tx1}	52.72 nF	R_{Tx1}	0.27 Ω
	L_{Tx2}	55.23 μH	C_{Tx2}	50.43 nF	R_{Tx2}	0.32 Ω
	L_{Tx3}	54.89 μH	C_{Tx3}	50.17 nF	R_{Tx3}	0.29 Ω
	L_{Tx4}	52.85 μH	C_{Tx4}	51.81 nF	R_{Tx4}	0.25 Ω
WPT system	L_{Tx5}	54.46 μH	C_{Tx5}	44.36 nF	R_{Tx5}	0.32 Ω
	L_{Tx6}	54.21 μH	C_{Tx6}	48.12 nF	R_{Tx6}	0.19 Ω
	L_{Tx7}	55.36 μH	C_{Tx7}	43.65 nF	R_{Tx7}	0.31 Ω
	L_{Tx8}	58.01 μH	C_{Tx8}	42.47 nF	R_{Tx8}	0.28 Ω
	L_{Tx9}	53.09 μH	C_{Tx9}	46.05 nF	R_{Tx9}	0.29 Ω
	Air gap	7 mm	C_{rec}	100 μF	R_L	10 Ω
Rx-I	L_{Rx1}	52.22 μH	C_{Rx1}	214.64 nF	R_{Rx1}	0.26 Ω
Rx-II	L_{Rx2}	113.92 μH	C_{Rx2}	23.49 nF	R_{Rx2}	0.35 Ω

Fig. 12.   Waveform of i_{Tx} in the coupling condition detecting process.

Rx-II is also put to verified the interoperability of the active-positioning scheme. As depicted in Fig. 11(d.1), the *Rx-II* is placed to cover coil 4 and 5, and it moves toward coil 7 and 8 straightly. In this case, coil 4 and 5 are energized and coil 7 and 8 are cut off at the first. *K7* and *K8* will be turned on when $\hat{i}_{Tx7}$ and $\hat{i}_{Tx8}$ are lower than φ, coli 4 and 5 will be cut off when $\hat{i}_{Tx4}$ and $\hat{i}_{Tx5}$ are higher than φ. The result under the case of *Rx-II* moving diagonally from zone 5 and 6 to zone 7 and 8 is shown in Fig. 11(d.2).

B. Verification of the Optimal Frequency Control Scheme

The proposed OFC scheme for efficiency optimization is also verified by both the *Rx-I* and *Rx-II*, and a total of three cases are studied. The results are shown in Fig. 13. The input dc voltage remains to be 24 V. In Fig. 13(x.1), the scale of the oscilloscope is 5 ms/div in time and 0.5 A/div in current. In Fig. 13(x.2) and (x.3), the scale of the oscilloscope is 5 μs/div in time, 0.5 A/div in current (i_{Tx}) and 1 V/div in voltage (PWMA).

As shown in Fig. 13(a.1), the *Rx-I* is placed in the middle of the *Tx* array. When coil 5 is selected to be energized after the active-positioning process, the digital circuit mentioned in Fig. 7 will start to detect the phase difference of i_{Tx} and PWMA. The control tolerance of this experiment is 1% (i.e., 3.6° of 360°). After the phase difference is detected and PWM-XOR is generated, a new switching frequency will be calculated and sent to the full-bridge inverter. In this case, the calculating time

is 6 ms, the phase difference is 40.32° (i_{Tx} leads v_{Tx}) under the original operating frequency 100 kHz and reduced to merely 1.16° after the frequency is tuned to the optimal frequency 150.4 kHz, as presented in Fig. 13(a.2) and (a.3). In the second case, *Rx-I* is placed to partially cover the coil 5, the tracking time for optimal frequency is 1.5 ms, the phase difference under the original frequency and optimal frequency 81.8 kHz is –49.67° (i_{Tx} legs behind v_{Tx}) and 2.66°, respectively, as depicted in Fig. 13(b). In Fig. 13(c), the *Rx-II* is placed to cover coil 4 and 5, and the calculating period is 3 ms. The phase difference under the initial state and the optimal frequency 115.9 kHz is 48.84° and 3.57°, respectively.

The system efficiency is also measured and compared in the three cases, and the results are drawn in Fig. 14. The system efficiency is measure by calculating the following equation:

$$\eta = \frac{\text{Re}\left[i_{Rx}^2 v_{Rx}\right]}{\text{Re}\left[v_{Tx} i_{Tx}\right]}. \tag{15}$$

It means the power loss in the inverter and rectifier is not involved for better demonstrating the performance of the proposed OFC scheme. As can be observed in Fig. 14, the optimal frequency always brings higher efficiency, and the improvement depends on the shape and position of the *Rx* and the input voltage. In all cases, the efficiency increases by up to 11.1%. The maximum improved efficiency occurs in case 2, where the *Rx* has obvious misalignment to the *Tx*, which indicates that the mutual inductance between the *Rx* and the *Tx* is lower. The original efficiency is much lower due to the weaker coupling, and thus the improvement is much more significant. The power loss is caused by the equivalent internal resistance of compensated capacitor, the copper resistance of the coil inductor, and also the residual uncompensated impedance.

C. Comparison Study Between the Proposed Scheme and Existing Methods

For depicting the advantages of the proposed method, a comparison on the key aspects, including sensor/(*Tx*+*Rx*) quantity, active switch/(*Tx*+*Rx*) quantity, power level, communication unit, maximum efficiency, OFC control scheme and resonance
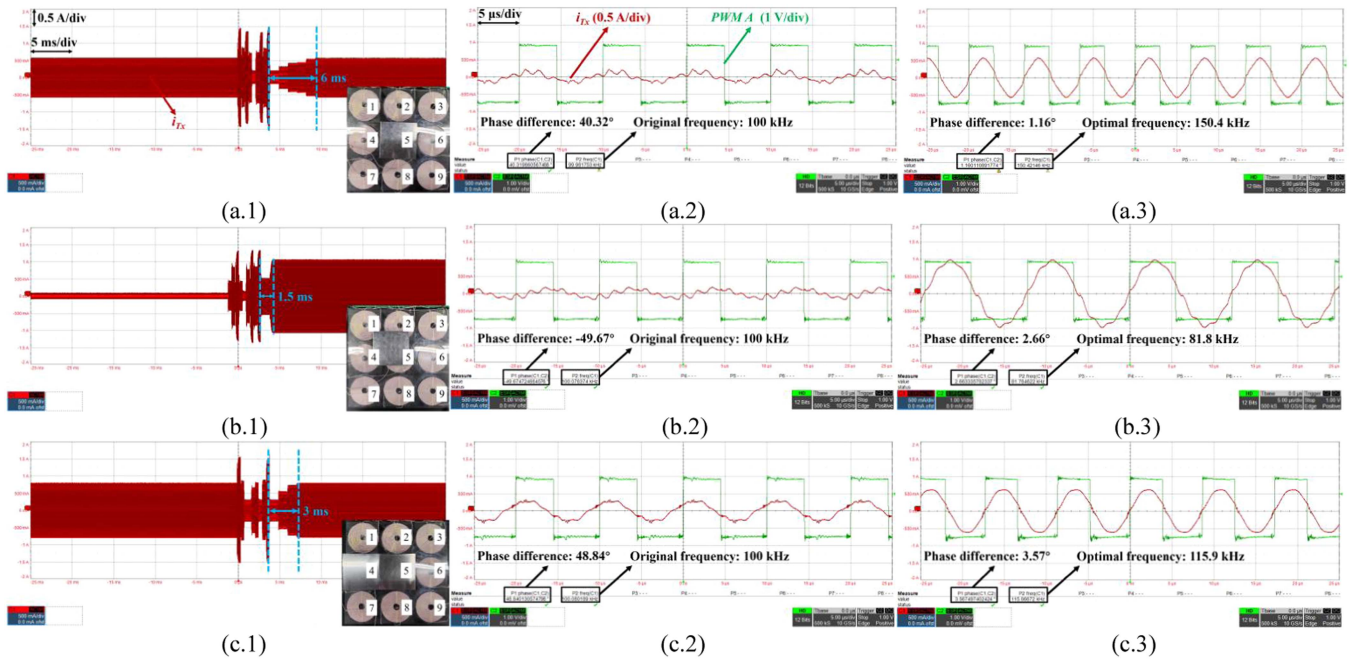
Fig. 13. Experimental waveforms of the OFC control with different placement of *Rxs*. (a) Case 1, *Rx-I* covering 1 *Tx*. (b) Case 2, *Rx-I* incompletely covering 1 *Tx*. (c) Case 3, *Rx-II* covering 2 *Txs*; (x.1) optimal frequency tracking process, (x.2) phase difference under original frequency, (x.3) phase difference under optimal frequency.

TABLE II
COMPARISON BETWEEN THIS ARTICLE AND THE PROPOSED RESEARCH

Ref No.	$\dfrac{\text{Hall sensor}}{Tx + Rx}$	$\dfrac{\text{Active swtich}}{Tx + Rx}$	Bi-directional Communication	Power level	Maximum efficiency	Dynamic response	OFC control scheme	Resonance condition recognition
[4]	1	3	Yes	300 W	85%	0.9-2 s	PSC	N.A.
[18]	0.5	2	No	80 W	80%	2 s	P&O	Parameter estimation
[19]	2	2	No	400 W	92%	2.7–3.6 s	PSC	N.A.
[24]	1	4	No	1000 W	96%	700 ms	PSC with PI loop	N.A.
[25]	1	3	No	100 W	90.2%	8–20 ms	P&O	No
This article	1	1.5	No	100 W	84.6%	1.5–6 ms	P&O with PI loop	Digital circuit

condition recognition with the other relevant research investigations are presented in Table II. The nominal power rating of the prototype in this article is 100 W, which is a comparable power level with other references. Meanwhile, based on the theoretical analysis in Sections II and III, the power level is not an impact to the control performance.

As compared with the DWC system with traditional PSC and P&O methods, the proposed control method has advantages of fast dynamic response, recognizable resonance condition, and low implementation cost. As there is no complicated parameter estimation and calculation, and no time delay from bidirectional

communication, the dynamic response of the proposed method is improved. Since the direction of optimal frequency sweeping should be determined based on the resonance condition, the traditional OFC based on P&O needs either parameter estimation [18] or large sweeping range in single direction [24]. The proposed method can recognize the resonance condition through a simple digital circuit which largely reduce the calculation and sweeping time. Meanwhile, the introduction of PI loop contributes to the acceleration of optimal frequency sweeping. Besides, the proposed control does not need excessive hall sensors and active switches (i.e., MOSFET in this study), and the
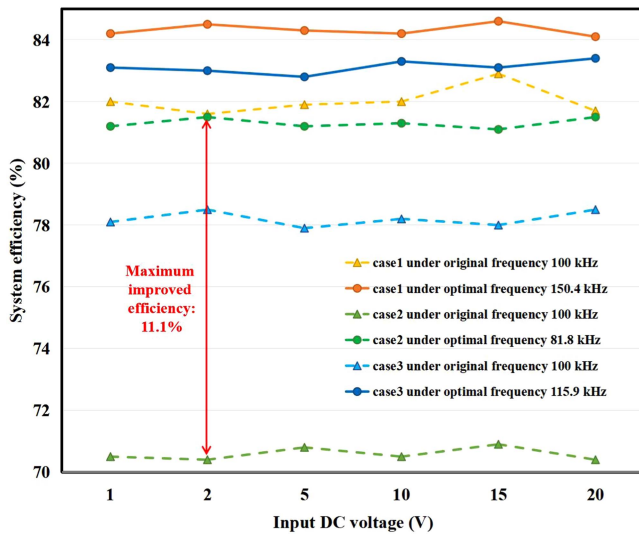
Fig. 14. Measured system efficiency in input voltage scale.

requirement, the dead zone, which may occur when the *Rx* is in the center of the adjacent *Tx*s, can be avoided, and thus the *Rx* can always have enough coupling in the operation. In the future, there are several aspects that can be further investigated based on this article.

1) The varied threshold value due to different load power. Although it is believed that the dc—dc converters are widely applied in the AGV side for power regulation [31], [32], [33], which would ensure the reflected impedance is a light load, the different operation conditions of the converters still could lead to the varied threshold value.

2) The concrete criteria of *Tx* module design should be further raised. Since the selection of the proper threshold value is related to the characteristics of the *Tx* configuration, the criteria of *Tx* module design should be studied. The *Tx* module should have less edges for avoiding undesired impulse of coupling coefficient, and the cross coupling should be minimized.

communication module and position sensor are not involved. The quantity of sensors and active switches utilized in this research maintains at 1 and 1.5 per coil, respectively, which is equal to or less than the majority of the compared research. A simple implementation of the system is proven. In the view of efficiency improving and controlling period, the proposed system can achieve ZPA for optimizing efficiency in 6 ms in the worst case, and the optimized efficiency is up to 84.6%.

V. CONCLUSION AND DISCUSSION

A positioning and optimal frequency control method for AGV DWC systems is proposed in this article. The proposed control scheme achieves *Rx* real-time positioning and OFC without any bidirectional communication, position sensor, and parameter estimation. The resonance condition is recognized by a simple digital circuit, and the fast frequency sweeping for ZPA is realized by introducing the PI loop. The reactive power in the primary side is significantly reduced by adopting frequency tuning, and thus the system efficiency is improved. Only one current sensor is required in the proposed control, which contributes to a simple, low-cost implementation. Experimental results prove that the proposed method has fast dynamic response, where the positioning process takes typically only 0.4 ms for each *Tx* coil, and the OFC can be achieved in 6 ms. The system efficiency can be increased by 11.1%, and the maximum efficiency is 84.6%. Two different *Rx*s with various movements are investigated in this article, and the similar performance is observed. It proves that the proposed method is with high interoperability to a DWC system for numerous kinds of AGVs. A benchmarking study is conducted by comparing the proposed method with relative references, and the comparison study shows that the proposed method have advantages of fast dynamic response, simple resonance condition recognition, and low implementation cost.

The proposed control method can be achieved when the *Rx* is in equal or larger size with the *Tx* module. By following the

REFERENCES

[1] H. Matsumoto, Y. Shibako, and Y. Neba, "Contactless power transfer system for AGVs," *IEEE Trans. Ind. Electron.*, vol. 65, no. 1, pp. 251–260, Jan. 2018.

[2] V. Digani, L. Sabattini, C. Secchi, and C. Fantuzzi, "Ensemble coordination approach in multi-AGV systems applied to industrial warehouses," *IEEE Trans. Automat. Sci. Eng.*, vol. 12, no. 3, pp. 922–934, Jul. 2015.

[3] S. Riazi, K. Bengtsson, and B. Lennartson, "Energy optimization of large-scale AGV systems," *IEEE Trans. Automat. Sci. Eng.*, vol. 18, no. 2, pp. 638–649, Apr. 2021.

[4] X. Dai, X. Li, Y. Li, and A. P. Hu, "Maximum efficiency tracking for wireless power transfer systems with dynamic coupling coefficient estimation," *IEEE Trans. Power Electron.*, vol. 33, no. 6, pp. 5005–5015, Jun. 2018.

[5] T. Fujita, T. Yasuda, and H. Akagi, "A dynamic wireless power transfer system applicable to a stationary system," *IEEE Trans. Ind. Appl.*, vol. 53, no. 4, pp. 3748–3757, Jul./Aug. 2017.

[6] F. Lu et al., "A tightly coupled inductive power transfer system for low-voltage and high-current charging of automatic guided vehicles," *IEEE Trans. Ind. Electron.*, vol. 66, no. 9, pp. 6867–6875, Sep. 2019.

[7] F. Lu et al., "A low-voltage and high-current inductive power transfer system with low harmonics for automatic guided vehicles," *IEEE Trans. Veh. Technol.*, vol. 68, no. 4, pp. 3351–3360, Apr. 2019.

[8] Z. Miao, D. Liu, and C. Gong, "Efficiency enhancement for an inductive wireless power transfer system by optimizing the impedance matching networks," *IEEE Trans. Biomed. Circuits Syst.*, vol. 11, no. 5, pp. 1160–1170, Oct. 2017.

[9] K. Chen, K. W. E. Cheng, Y. Yang, and J. Pan, "Stability improvement of dynamic EV wireless charging system with receiver-side control considering coupling disturbance," *Electronics*, vol. 10, 2021, Art. no. 1639.

[10] S. Y. Choi, B. W. Gu, S. Y. Jeong, and C. T. Rim, "Advances in wireless power transfer systems for roadway-powered electric vehicles," *IEEE J. Emerg. Sel. Topics Power Electron.*, vol. 3, no. 1, pp. 18–36, Mar. 2015.

[11] C. Kaiwen, L. Junyuan, O. Yuzhao, J. Yipeng, J. F. Pan, and E. K.-W. Cheng, "Coupling tracking and control in the dynamic wireless charging for electric vehicles," in *Proc. 8th Int. Conf. Power Electron. Syst. Appl.*, 2020, pp. 1–5, doi: 10.1109/PESA50370.2020.9344043.

[12] G. Wei, X. Jin, C. Wang, J. Feng, C. Zhu, and M. I. Matveevich, "An automatic coil design method with modified AC resistance evaluation for achieving maximum coil–coil efficiency in WPT systems," *IEEE Trans. Power Electron.*, vol. 35, no. 6, pp. 6114–6126, Jun. 2020.

[13] M. Mohammad, S. Choi, Z. Islam, S. Kwak, and J. Baek, "Core design and optimization for better misalignment tolerance and higher range of wireless charging of PHEV," *IEEE Trans. Transp. Electrific.*, vol. 3, no. 2, pp. 445–453, Jun. 2017.

[14] P. Zhang, M. Saeedifard, O. C. Onar, Q. Yang, and C. Cai, "A field enhancement integration design featuring misalignment tolerance for wireless EV charging using LCL topology," *IEEE Trans. Power Electron.*, vol. 36, no. 4, pp. 3852–3867, Apr. 2021.

[15] Y. Chen, H. Zhang, C.-S. Shin, C.-H. Jo, S.-J. Park, and D.-H. Kim, "An efficiency optimization-based asymmetric tuning method of double-sided LCC compensated WPT system for electric vehicles," *IEEE Trans. Power Electron.*, vol. 35, no. 11, pp. 11475–11487, Nov. 2020.

[16] P. Darvish, S. Mekhilef, and H. A. B. Illias, "A novel *S–S–LCLCC* compensation for three-coil WPT to improve misalignment and energy efficiency stiffness of wireless charging system," *IEEE Trans. Power Electron.*, vol. 36, no. 2, pp. 1341–1355, Feb. 2021.

[17] X. Dai, J.-C. Jiang, and J.-Q. Wu, "Charging area determining and power enhancement method for multiexcitation unit configuration of wirelessly dynamic charging EV system," *IEEE Trans. Ind. Electron.*, vol. 66, no. 5, pp. 4086–4096, May 2019.

[18] S.-J. Huang, T.-S. Lee, W.-H. Li, and R.-Y. Chen, "Modular on-road AGV wireless charging systems via interoperable power adjustment," *IEEE Trans. Ind. Electron.*, vol. 66, no. 8, pp. 5918–5928, Aug. 2019.

[19] A. Zakerian, S. Vaez-Zadeh, and A. Babaki, "A Dynamic WPT system with high efficiency and high power factor for electric vehicles," *IEEE Trans. Power Electron.*, vol. 35, no. 7, pp. 6732–6740, Jul. 2020.

[20] Z. Yan et al., "Frequency optimization of a loosely coupled underwater wireless power transfer system considering eddy current loss," *IEEE Trans. Ind. Electron.*, vol. 66, no. 5, pp. 3468–3476, May 2019.

[21] J. M. Miller, O. C. Onar, and M. Chinthavali, "Primary-side power flow control of wireless power transfer for electric vehicle charging," *IEEE J. Emerg. Sel. Topics Power Electron.*, vol. 3, no. 1, pp. 147–162, Mar. 2015.

[22] A. Koran and K. Badran, "Adaptive frequency control of a sensorless-receiver inductive wireless power transfer system based on mixed-compensation topology," *IEEE Trans. Power Electron.*, vol. 36, no. 1, pp. 978–990, Jan. 2021.

[23] E. S. Lee, "Frequency modulation based IPT with magnetic communication for EV wireless charging," *IEEE Trans. Ind. Electron.*, vol. 70, no. 2, pp. 1398–1408, Feb. 2023.

[24] Y. Liu, U. K. Madawala, R. Mai, and Z. He, "Zero-phase-angle controlled bidirectional wireless EV charging systems for large coil misalignments," *IEEE Trans. Power Electron.*, vol. 35, no. 5, pp. 5343–5353, May 2020.

[25] K. Chen, K. W. E. Cheng, Y. Yang, and J. Pan, "A fast self-positioning-based optimal frequency control for inductive wireless power transfer systems without communication," *IEEE Trans. Ind. Electron.*, vol. 70, no. 1, pp. 334–343, Jan. 2023.

[26] E. S. Lee and S. H. Han, "2-D thin coil designs of IPT for wireless charging of automated guided vehicles," *IEEE J. Emerg. Sel. Topics Power Electron.*, vol. 10, no. 2, pp. 2629–2644, Apr. 2022.

[27] E. S. Lee, M. Y. Kim, S. M. Kang, and S. H. Han, "Segmented IPT coil design for continuous multiple charging of an electrified monorail system," *IEEE Trans. Power Electron.*, vol. 37, no. 3, pp. 3636–3649, Mar. 2022.

[28] S. R. Khan, S. K. Pavuluri, and M. P. Y. Desmulliez, "Accurate modeling of coil inductance for near-field wireless power transfer," *IEEE Trans. Microw. Theory Techn.*, vol. 66, no. 9, pp. 4158–4169, Sep. 2018.

[29] J. Lu, G. Zhu, D. Lin, Y. Zhang, H. Wang, and C. C. Mi, "Realizing constant current and constant voltage outputs and input zero phase angle of wireless power transfer systems with minimum component counts," *IEEE Trans. Intell. Transp. Syst.*, vol. 22, no. 1, pp. 600–610, Jan. 2021.

[30] Y. Yang, S. C. Tan, and S. Y. R. Hui, "Fast hardware approach to determining mutual coupling of series–series-compensated wireless power transfer systems with active rectifiers," *IEEE Trans. Power Electron.*, vol. 35, no. 10, pp. 11026–11038, Oct. 2020.

[31] K. Chen, J. Pan, Y. Yang, and K. W. E. Cheng, "Stability improvement and overshoot damping of SS-compensated EV wireless charging systems with user-end buck converters," *IEEE Trans. Veh. Technol.*, vol. 71, no. 8, pp. 8354–8366, Aug. 2022.

[32] J. Liu, Z. Liu, and H. Su, "Passivity-based PI control for receiver side of dynamic wireless charging system in electric vehicles," *IEEE Trans. Ind. Electron.*, vol. 69, no. 1, pp. 783–794, Jan. 2022.

[33] Z. Zhou, L. Zhang, Z. Liu, Q. Chen, R. Long, and H. Su, "Model predictive control for the receiving-side DC-DC converter of dynamic wireless power transfer," *IEEE Trans. Power Electron.*, vol. 35, no. 9, pp. 8985–8997, Sep. 2020.

Kaiwen Chen (Member, IEEE) was born in Zhejiang, China. He received the B.Eng. degree in electrical engineering and automation from the Harbin Institute of Technology, Harbin, China, in 2016, and the M.Sc. and Ph.D. degrees in electrical engineering from Hong Kong Polytechnic University, Hong Kong, in 2017 and 2022, respectively.

His main research interests include dynamic wireless power transfer, electric vehicles, and control theory.

Yuzhao Ouyang received the B.S. degree in rail transit signal and control from Linyi University, Linyi, China, and the M.S. degree in electronic information from Shenzhen University, Shenzhen, China.

His research interests include design and control of wireless power transfer systems.

Xiaodong Yang received the B.S. degree in electrical engineering from the Henan Institute of Science and Technology, Henan, China. He is currently working toward the M.S. degree in control engineering from the College of Mechatronics and Control Engineering, Shenzhen University, Shenzhen, China.

His research interests include design and analysis of wireless power transfer technologies.

Norbert Chow Cheung (Senior Member, IEEE) received the B.Sc. degree in electrical and electronics engineering from Queen Marry College, London University, London, U.K., the M.Sc. degree in electrical engineering from the University of Hong Kong, Hong Kong, and the Ph.D. degree in electrical engineering from the University of New South Wales, Sydney, NSW, Australia, in 1981, 1987, and 1995, respectively.

He is currently working with the College of Mechatronics and Control Engineering, Shenzhen University, Shenzhen, China. His research interests include actuators design, motion control, and robotics.
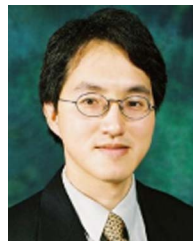
Eric Ka-Wai Cheng (Fellow, IEEE) received the B.Sc. and Ph.D. degrees in electronic & electrical engineering from the University of Bath, Bath, U.K., in 1987 and 1990, respectively.

He is currently a Professor and the Director of the Power Electronics Research Centre, Faculty of Engineering, Department of Electrical Engineering, The Hong Kong Polytechnic University, Hong Kong. He has authored or coauthored more than 400 articles and 7 books. His research interests include all aspects of power electronics, electromagnetic interference, electric vehicles, and wireless power transfer.

Jianfei Pan (Member, IEEE) received the Ph.D. degree in electrical engineering from the Department of Electrical Engineering, Hong Kong Polytechnic University, Hong Kong, in 2006.

He is currently working with the College of Mechatronics and Control Engineering, Shenzhen University, Shenzhen, China. His main research interests include wireless power transfer, and electric machine design and control.